Characteristics of electron internal transport barrier in Heliotron J

N Kenmochi[1], T Minami[2], C Takahashi[2], S Mochizuki[3], K Nishioka[4], S Kobayashi[2], K Nagasaki[2], Y Nakamura[3], H Okada[2], S Kado[2], S Yamamoto[2], S Ohshima[2], S Konoshima[2], G M Weir[5], Y Otani[3], T Mizuuchi[2]

[1]Graduate School of Frontier Sciences, The University of Tokyo, Kashiwa, Chiba 277-8561, Japan
[2]Institute of Advanced Energy, Kyoto University, Uji, Kyoto 611-0011, Japan
[3]Graduate School of Energy Science, Kyoto University, Uji, Kyoto 611-0011, Japan
[4]Department of Physics, Nagoya University, Nagoya, Aichi 464-8602, Japan
[5]Max-Planck-Institut für Plasmaphysik, Tailinstitut Greifswald, EURATOM Association, Wendelsteinstr. 1, Greifswald 17491, Germany

E-mail: kenmochi@ppl.k.u-tokyo.ac.jp

December 2016

Abstract. The formation of an electron internal transport barrier (eITB) has been observed for the first time with centrally focused electron cyclotron heating (ECH) microwaves injected into plasma in Heliotron J. When the heating power per electron density ($P_{\rm ECH}/\bar{n_e}$) exceeds a threshold of 250×10^{-19}kW m^3, transient increases of both the central T_e and the core T_e gradients are observed. A neoclassical (NC) calculation using the Sugama-Nishimura moment method predicts that the large positive radial electric field (E_r) is formed in the core region. Heat transport analysis shows a significant reduction of the effective electron thermal diffusivity in the plasma with the eITB related to that without the eITB. The large gap between the experimentally obtained effective thermal diffusivity and the NC thermal diffusivity suggests that the suppression of anomalous transport contributes to the core improved confinement of the eITB plasma. The electron cyclotron emission measurement shows both the transient increase and the hysteresis phenomena during the eITB formation.

Submitted to: *Plasma Phys. Control. Fusion*

1. Introduction

The electron internal transport barrier (eITB) formation has been observed in several stellarator/heliotron devices[1, 2, 3, 4]. It is thought that the eITB is characterized by the transitions between the "ion root" (with a small magnitude of radial electric field(E_r), usually negative) and the "electron root" (with a large positive E_r) that are

based on a bifurcation mechanism[5]. According to this feature, in LHD and CHS, a large positive E_r in the core region and a transient formation of a peaked electron temperature (T_e) profile with a density and a heating power threshold are observed when an eITB is formed[6, 7].

The effects of the magnetic field configuration on eITB formations, particularly in terms of the effective helical ripple (ϵ_{eff})[5] and magnetic islands[8, 9, 10], have been observed. In contrast, the mechanism of the effect of such a magnetic configuration is not well studied. Various types of stellarator/heliotron devices exploit unique concepts for the optimization study of the helical configuration. While LHD and CHS have a strong variation of ι (strong shear) to reduce the island width, Heliotron J, TJ-II, HSX, and W7-X have almost flat ι profiles (shearless) close to (but outside) the low order rationals, where the density of the rational numbers is smaller. A comparative study between these stellarator/heliotron devices can contribute to the elucidation of the mechanism of magnetic field configuration effect on the eITB physics.

Heliotron J belongs to the extended family of the "quasi-isodynamic symmetric optimization" devices, where a continuous $L = 1$ helical winding is used instead of modular coils. The helical-axis heliotron creates a vacuum magnetic well in the entire confinement region by using an advanced three-dimensional (3D) magnetic axis. Heliotron J is a medium-sized helical-axis heliotron device (the averaged plasma major radius is $R = 1.2$ m, the averaged minor radius is $a = 0.17$ m, and the averaged magnetic field strength at the magnetic axis is $B_{\rm ax} = 1.35$ T) with an $L/M = 1/4$ helical coil, where L and M are the pole number and pitch numbers of the helical coil, respectively[11, 12] . The Boozer magnetic field spectrum is varied with two sets of toroidal coils, inner vertical coil, outer vertical coil, and external vertical coil connected to the helical coil. This flexible helical axis heliotron device allows the study of core confinement in a wide configuration space. This research aims at identifying the eITB formation and revealing the detailed characteristics of the eITB in the helical-axis heliotron configuration, namely the unique configuration of Heliotron J. The characteristics are investigated from the profiles of T_e and E_r, formation condition, and heat transport by using an advanced electron cyclotron heating (ECH) system and various diagnostics and by comparing the obtained results to those for the other helical devices. The research of eITB physics in the helical-axis heliotron configuration contributes to expand the variety of configuration research in the stellarator/heliotron devices.

Section 2 discusses the eITB profile characteristics in Heliotron J. An eITB formation condition is investigated in terms of n_e in Section 3, and the estimation of a neoclassical (NC) E_r using the Sugama-Nishimura moment method[13, 14] is described in Section 4. In Section 5, the heat transport of the eITB is analyzed using the experimental results and the experimental heat transport and the NC heat transport are compared. Section 6 illustrates temporal dynamics during the eITB formation using the electron cyclotron emission (ECE) measurements. Finally, conclusions are presented in Section 7.

2. Typical Characteristics of Plasma with Peaked Temperature Profile in Heliotron J

Plasmas are produced and heated by ECH in Heliotron J. The ECH system of Heliotron J can continuously vary the injection power $P_{\rm ECH}$ during a single discharge. The continuous control enables the investigations of the plasma response for wide heating power range, which is useful for studying of the dynamics of plasma transport. While ECH modulation techniques are used in the heat pulse propagation experiments, few experimental results have been reported for plasma dynamics with continuously varied ECH. The continuously varied ECH enables the investigations of the transition and back-transition for the eITB regime during a single shot. Due to the NC bifurcation characteristics of the helical plasma, hysteresis during eITB formation has been reported for E_r in CHS[15] and W7-AS[16]. The continuously varied ECH is also effective for studying hysteresis phenomena.

A peaked T_e profile is observed with an on-axis ECH. Here, we show the typical peaked and non-peaked T_e plasmas obtained in a single plasma discharge by changing $P_{\rm ECH}$. The second-harmonic 70 GHz ECH beam with the extraordinary mode is perpendicularly injected in the experiment. The parallel refractive index $N_{||}$ is set to approximately 0.0 and the magnetic field strength is adjusted such that the EC power absorption can be peaked on the axis. In this heating condition, the electron cyclotron driven current (ECCD) is nearly zero and the bootstrap current of only several kA is observed. The vacuum central iota is $\iota(0)/2\pi \sim 0.56$ and the magnetic configuration is set to avoid placing the low order resonances in the core region. In this experiment, $P_{\rm ECH}$ is controlled by temporally changing the gyrotron beam voltage for a constant n_e plasma. Figure 1(a) shows the time evolution of the line-averaged electron density $\bar{n_e}$, the plasma stored energy W_p^{dia}, and $P_{\rm ECH}$. In the ECH power control experiment, $P_{\rm ECH}$ is controlled to be gradually reduced from 330 to 120 kW after $t = 210$ ms under the constant $\bar{n_e} \sim 1.0 \times 10^{19}$ m^{-3}. W_p^{dia} slightly decreases as $P_{\rm ECH}$ is reduced. Figures 1(b) and 1(c) show the typical T_e and n_e profiles with $P_{\rm ECH}$ values of 175 and 240 kW, respectively. Here, the T_e and n_e profiles are measured using a Nd:YAG laser Thomson scattering (YAG-TS) system[17, 18]. In this plasma condition, the n_e is sufficiently high for neglecting the effects of the high energy electrons on the T_e measurement. The n_e profiles are nearly identical for the two heating power cases. On the other hand, different T_e profile shapes are observed during the $P_{\rm ECH}$ change. The maximum value of central T_e [$T_e(0)$] reaches 1.5 keV with $P_{\rm ECH} = 240$ kW with the steep T_e gradient of 30 keVm^{-1} at $r/a = 0.2$. A high T_e region is created around the center ($r/a < 0.3$). Moreover, the reduction of $P_{\rm ECH}$ results in a decreased T_e gradient in the core region ($r/a < 0.3$), while the T_e in the outer region ($r/a > 0.3$) is almost identical for the two heating power cases [see Figs. 1(b) and 1(c)].

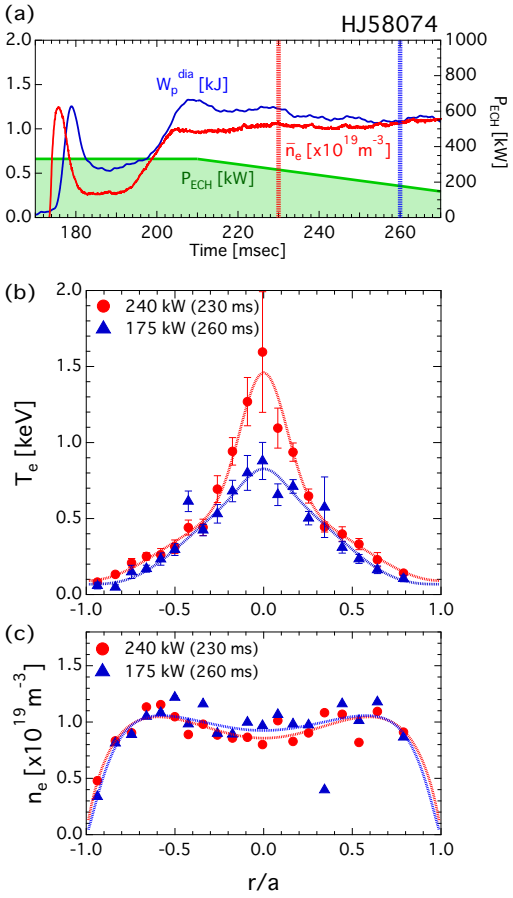

Figure 1. (a) Time evolution of the plasma stored energy, line-averaged electron density, and electron cyclotron heating (ECH) injection power. Profiles of (b) T_e and (c) n_e with ECH (injection power: 175 and 240 kW).

3. Density Threshold for eITB Formation

To explore the conditions for the formation of the peaked T_e profiles, we investigate the density dependence on central T_e and the T_e gradient. In this experiment, we control n_e by changing gas-puff fueling under a constant $P_{\rm ECH}$. Figure 2(a) shows the time evolution of $\bar{n_e}$, W_p^{dia}, and $P_{\rm ECH}$. Figures 2(b) and 2(c) show the typical T_e and n_e profiles. The peaked T_e profile in the plasma core ($r/a < 0.2$) disappears in the case of high n_e, while the profile shape of the outer region ($r/a > 0.2$) does not vary in the experiment [see Figs. 2(b) and 2(c)]. The maximum value of $T_e(0)$ reaches 2 keV with a steep T_e gradient.

Here, the T_e profiles are fitted using the following function.

$$\frac{T_e(\rho)}{T_e(0)} = g - h + \frac{1-g+h}{(1-\rho^p)^q} + h\left\{1 - \exp\left(\frac{-\rho^2}{w^2}\right)\right\}, \qquad (1)$$

where $\rho = r/a$, $g = T_e(1)/T_e(0)$, and h and w are the hole depth and width, respectively. In this equation, $T_e(\rho)$ denotes radial T_e profiles. The central and peripheral ($r/a = 0.5$)

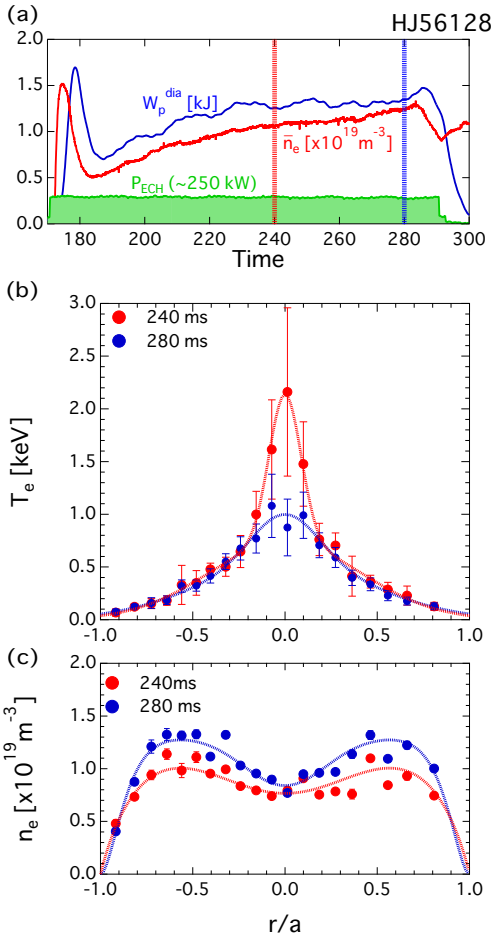

Figure 2. (a) Time evolution of the plasma stored energy, line-averaged electron density, and ECH injection power. Profiles of (b) T_e and (c) n_e at 240 and 280 ms, respectively.

T_e are plotted as a function of $\bar{n_e}$ in Fig. 3. Clear transitions are observed for both T_e and T_e gradients. As $\bar{n_e}$ decreases below the threshold value($1.1-1.3\times10^{19}$ m^{-3}), central T_e increases significantly, and the T_e shape is transformed to the peaked profile. Central T_e increases to 3 keV at the low $\bar{n_e} \sim 0.6\times10^{19}$ m^{-3}, while the T_e variation of the peripheral region is small. The T_e gradient at the core region shows the same transient increase as that shown by T_e. When $\bar{n_e}$ is below the threshold density ($1.1-1.3\times10^{19}$ m^{-3}), the T_e gradient at $r/a = 0.1$ increases from approximately 20 to approximately 80 keV/m. In contrast, the gradient at $r/a = 0.3$ is nearly constant at approximately 10 keV/m. The difference in the T_e gradient responses for the n_e change between the core and peripheral regions shows that there is a clear difference of the transport characteristics between the two regions. The difference between the T_e profiles is also observed in the ECH power control experiment described in Section 2. The findings that both higher $P_{\rm ECH}$ and lower n_e contribute to the formation of the peaked profile are consistent with the predictions that the ion-electron root transition occurs in the collisionless regime and

in a plasma with a high T_e/T_i ratio, respectively. The transient increase of both T_e and T_e gradient suggest that these phenomena have bifurcation nature explained by the NC theory.

In LHD, the large size of helical device ($R \sim 3.6$ m), the clear transition of T_e and T_e gradient have also been observed, while the normalized threshold value of $P_{\rm ECH}/\bar{n_e}$ for the eITB formation is larger (approximately 700×10^{-19}kWm^3) than that of Heliotron J (approximately 250×10^{-19}kWm^3)[19, 20]. The much higher helical field ripple in the core region caused by the strong helical axis of Heliotron J (factor of 25 compared to LHD) could increase the ripple transport of the electrons and decrease $P_{\rm ECH}/\bar{n_e}$ at which the eITB formation occurs. ϵ_{eff}, which indicates the property of the NC helical ripple transport in the $1/\nu$ regime, is a candidate for understanding the differences between the threshold values[21]. Table 1 lists the threshold values of $P_{\rm ECH}/\bar{n_e}$ of the stellarator/heliotron devices and their characteristics including ϵ_{eff} in the ascending order of $P_{\rm ECH}/\bar{n_e}$. In the table, we calculate the threshold value of $P_{\rm ECH}/\bar{n_e}$ referring to the reports for each device. A comparison of Heliotron J ($\epsilon_{eff}(\rho = 0.2) \sim 0.1$), W7-AS ($\epsilon_{eff}(\rho = 0.2) \sim 0.016$), and LHD ($\epsilon_{eff}(\rho = 0.2) \sim 0.009$ or 0.004) shows that larger ϵ_{eff} corresponds to smaller threshold values and therefore easier eITB formation. While the explanation is certainly plausible, in CHS which has nearly the same magnetic configuration as that of LHD, the threshold value of $P_{\rm ECH}/\bar{n_e} \sim 260 \times 10^{-19}$kWm^3 is nearly the same as that of Heliotron J[22]. Furthermore, a comparison of CHS ($\epsilon_{eff}(\rho = 0.2) \sim 0.01$), W7-AS ($\epsilon_{eff}(\rho = 0.2) \sim 0.016$), and TJ-II ($\epsilon_{eff}(\rho = 0.2) \sim 0.07$) shows that the trend in the threshold values is opposite to the order expected based on ϵ_{eff}. Therefore, additional factors that determine the threshold value may exist, such as the presence of a magnetic island. For LHD[23] and TJ-II[24], the effects of the magnetic island on plasma flow, turbulence, and heat transport were investigated, and it was reported that the existence of a magnetic island triggers the eITB formation. The effects of a magnetic island on the eITB formation are also under investigation in Heliotron J.

4. Estimation of a NC Radial Electric Field

In stellarator/heliotron devices, the NC theory predicts a large E_r in the core region in an eITB plasma, with the experimental results supporting the NC predictions[5]. A NC calculation is conducted using the moment method (Sugama-Nishimura's method)[13, 14] to estimate the E_r value for the peaked profile. The magnitude of the NC ambipolar $E_{\rm r}$ is reported to be in good agreement with the measured $E_{\rm r}$ in stellarator/heliotron devices.

We calculate E_r using the T_e and n_e profiles with the peaked T_e plasma, as shown in Fig. 1 ($P_{\rm ECH} = 240$ kW). In this calculation, we assume the ion temperature profile as $T_i(r) = 150(1 - (r/a)^{1.57})^{1.11}$ (in eV), the typical profile of the Heliotron J plasma whose validity has been previously confirmed by charge exchange recombination spectroscopy(CXRS)[27]. Due to the nonlinear dependence of the NC particle fluxes on

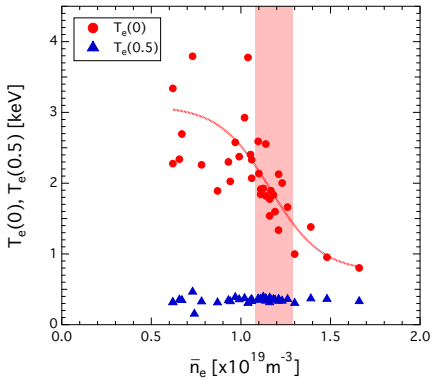

Figure 3. Density dependence on central($r/a = 0$) and peripheral($r/a = 0.5$) T_e.

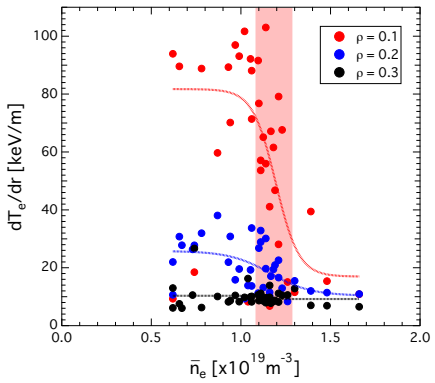

Figure 4. Density dependence on the T_e gradient (at $\rho = 0.1$, 0.2, and 0.3 ($\rho = r/a$)).

Table 1. Threshold power/density and parametric overview of stellarator/heliotron devices.

Device	Magnetic configuration	Major/minor radius	Rotational transform	Effective helical ripple	Threshold power/density	Ref.
		R/a [m]	$\iota(0)/2\pi$	$\epsilon_{eff}(\rho = 0.2)$	$P_{\rm ECH}/\bar{n_e}$ [10^{-19}kWm^3]	
Heliotron J	Helical-axis heliotron	1.2/0.17	0.56	~ 0.1	~ 250	[11, 12]
CHS	Heliotron	0.92/0.19	0.31	~ 0.01	~ 260	[22]
W7-AS	Helias	2.0/0.18	0.4	~ 0.016	~ 400	[1, 25]
TJ-II	Heliac	1.5/0.2	1.51	~ 0.07	$\sim 500 - 750$	[4, 25]
LHD($R_{\rm ax}$=3.5)	Heliotron	3.5/0.6	0.4	~ 0.009	~ 700	[20]
LHD($R_{\rm ax}$=3.75)		3.75/0.59	0.35	~ 0.004	~ 1400	[26]

E_r in the helical plasma, E_r is determined by the ambipolar condition as follows:

$$\Gamma_e(E_r) = \Gamma_i(E_r), \tag{2}$$

where Γ represents the particle flux of the plasma species with "e" for electrons and "i" for ions. In Figs. 5(a)-5(c), the calculated Γ_i and Γ_e are plotted as a function of E_r at $r/a = 0.17$, 0.5 and 0.77 for the peaked T_e plasma. At $r/a = 0.77$ [Fig. 5(a)], the ambipolarity provides the ion-root E_r. An increase of T_e in the core region leads to the rapid growth in Γ_e. When T_e reaches a value larger than that in the radial inner region, the second solution for a large positive E_r appears (the third solution appears simultaneously but is thermodynamically unstable) [Fig. 5(b)]. This solution is called the *electron root*. A further increase in core T_e at $r/a = 0.17$ leads to the further growth in Γ_e and only the electron root appears [Fig. 5(c)]. Figure 6(b) shows the radial profiles of the theoretically expected ambipolar E_r of both the peaked and non-peaked plasmas. For both plasmas, only the electron root (large positive E_r) is predicted in the core region ($r/a < 0.3$), while the electron and ion roots are predicted to coexist in the outer region ($0.3 < r/a < 0.6$). The experimentally obtained T_e profile is sufficient for considering the ion-electron root transition. A large positive E_r(12 kV/m) is expected for the peaked T_e profile while the value of E_r is nearly half (5 kV/m) for that of the non-peaked T_e profile, as shown in Fig. 6(b). The Bohm and gyro-Bohm mixed transport model with the $\mathbf{E} \times \mathbf{B}$ shear flow effect has already been compared to the helical and tokamak experimental ITBs[28, 29]. The most widely accepted explanation for the ITB formation relies on the suppression of TEM or ITG turbulence due to the $\mathbf{E} \times \mathbf{B}$ shear flow. The turbulence suppression may occur when the $\mathbf{E} \times \mathbf{B}$ flow shearing rate $\omega_{\mathbf{E}\times\mathbf{B}}$ exceeds the linear growth rate of these turbulences. In our case (Fig. 6), it is possible that the $\omega_{\mathbf{E}\times\mathbf{B}}$ of the peaked T_e plasma exceeds these growth rates while the positive E_r is formed.

This calculation result and measured T_e profile suggest that (1) the large positive E_r similar to that observed in other stellarator/heliotron devices can form in Heliotron J and (2) the E_r is sufficiently large for suppressing both the NC transport and the turbulence.

5. Heat Transport Characteristics and Comparison with NC Calculation

5.1. Heat Transport Analysis Using Experimental Results

The analysis of heat transport characteristics is indispensable for identifying eITB. We estimate the electron thermal diffusivities for the ECH power control experiment. The effective electron thermal diffusivity (χ_e^{eff}) profiles are evaluated using the T_e and n_e profiles obtained from the YAG-TS measurement and the single-pass ECH deposition profiles Q_ECH for the cases of $P_\mathrm{ECH} \sim 240$ and 175 kW (Fig. 7). χ_e^{eff} is defined as follows:

$$\chi_e^{eff}(r/a) = \frac{Q_\mathrm{ECH}}{n_e \nabla T_e}. \tag{3}$$

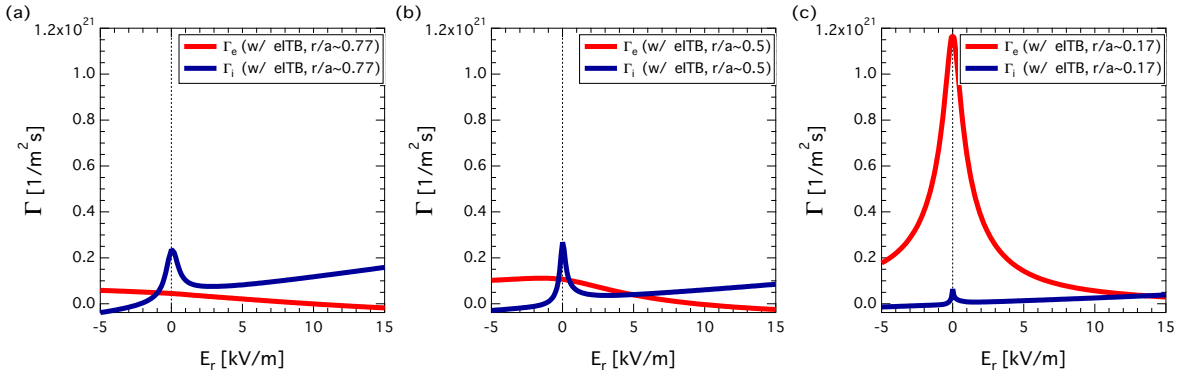

Figure 5. Neoclassical(NC) ion (Γ_i) and electron (Γ_e) fluxes as a function of E_r at (a)$r/a = 0.77$ (outside the foot point), (b) $r/a = 0.5$, and (c) $r/a = 0.17$ (inside the foot point). $\Gamma_i = \Gamma_e$ provides ambipolar E_r.

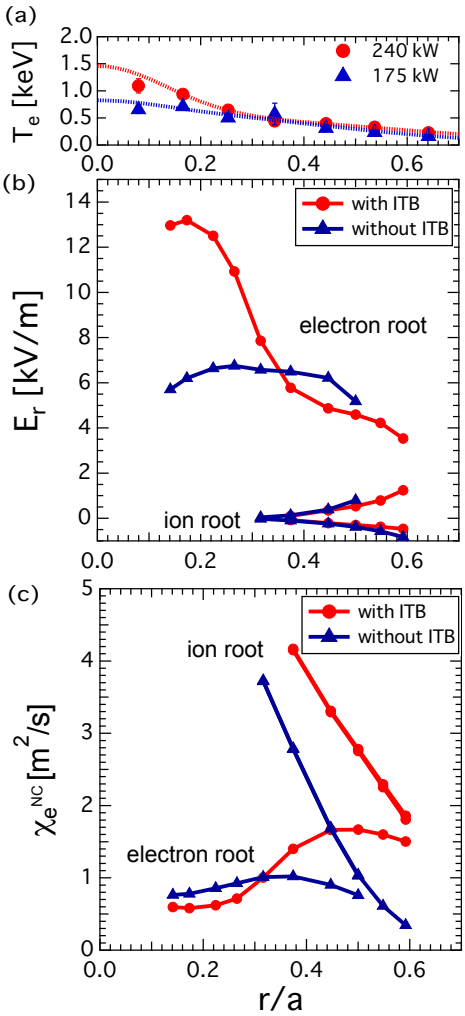

Figure 6. Results of NC calculation using the moment method for the peaked and non-peaked plasmas. Radial profiles of (a) the T_e, (b) the E_r, and (c)the electron thermal-diffusivity profiles.

Here, the $Q_{\rm ECH}$ is calculated using the TRAVIS ray-tracing code[30, 31]. TRAVIS is a ray-tracing code for ECH/ECCD and ECE diagnostics in arbitrary 3D magnetic configurations. The code has been applied and validated for Heliotron J[31]. Figure 7(a) shows the calculated $Q_{\rm ECH}$ for the peaked and non-peaked plasmas for the ECH power control experiment shown in Fig. 1. In this estimation of χ_e^{eff}, we neglect the electron-ion energy transfer and the impurity radiation losses, for which the contributions are considered to be negligible, particularly in the core region. The uncertainty in χ_e^{eff} is due to the uncertainties in the T_e and n_e profile measurements.

For a low injection power of 175 kW, χ_e^{eff} does not significantly change in the entire plasma region because of the constant T_e gradient. For the 240 kW case, χ_e^{eff} drastically decreases from 10 m^2/s (at $r/a \sim 0.4$) to 4 m^2/s (at $r/a \sim 0.2$), which is a direct reflection of the steep T_e gradient as shown in Fig. 7(a). However, in the outer region ($r/a > 0.3$) χ_e^{eff} is high compared to χ_e^{eff} for the case of $P_{\rm ECH}$ ~175 kW. The T_e gradient does not increase while the $P_{\rm ECH}$ increases, suggesting the degradation of peripheral confinement. This phenomenon is well known as the feature of power degradation in the L-mode confinement. The transport analysis shows a clear reduction of χ_e^{eff} for $r/a < 0.3$ in the highly peaked T_e profile case suggesting improved confinement in the core region.

A comparative study of experimental and NC theory results provides more detailed information about the transport properties of the peaked T_e plasma. For this purpose, the NC calculation is performed using the method described in Section 4, which considers the calculated E_r. In this calculation, we discuss the plasmas in the ECH power control experiment shown in Fig. 1 ($P_{\rm ECH}$ = 175, and 240 kW). Figure 6(c) shows the NC prediction of the electron thermal diffusivity (χ_e^{NC}). The χ_e^{NC} of the peaked plasma is lower than that of the non-peaked plasma in the core region ($r/a < 0.3$). However, the difference of χ_e^{NC} between the peaked and non-peaked plasmas in the core region ($r/a < 0.3$) is small compared to that of χ_e^{eff}. χ_e^{NC} and χ_e^{eff} are plotted in Fig. 7. In the core region, χ_e^{NC} for the peaked plasma is approximately 1/7 times smaller than χ_e^{eff} for the peaked plasma. As the experimentally obtained χ_e^{eff} contains the effects of both NC and anomalous transport, the difference in χ_e^{eff} between the peaked and non-peaked plasmas is attributed to the reduction of the anomalous transport in the core region.

5.2. Evaluation of Turbulence Suppression

To quantitatively evaluate the degree of reduction of anomalous transport, we investigate the dependence of χ_e^{eff} on T_e. Figure 8(a) shows χ_e^{eff} as a function of T_e inside and outside the foot point. Here, the foot point is defined as the point where the rate of the change in the T_e gradient ($d^2T_e/d\rho^2; \rho = r/a$) reaches the maximum value. The T_e dependence of χ_e^{eff} is clearly different inside and outside the foot point. Outside the foot point, χ_e^{eff} increases as T_e increases, following the relation of $\chi_e^{eff} \propto T_e^{1.9}$. In contrast, χ_e^{eff} sharply decreases inside the foot point as T_e increases with the relation

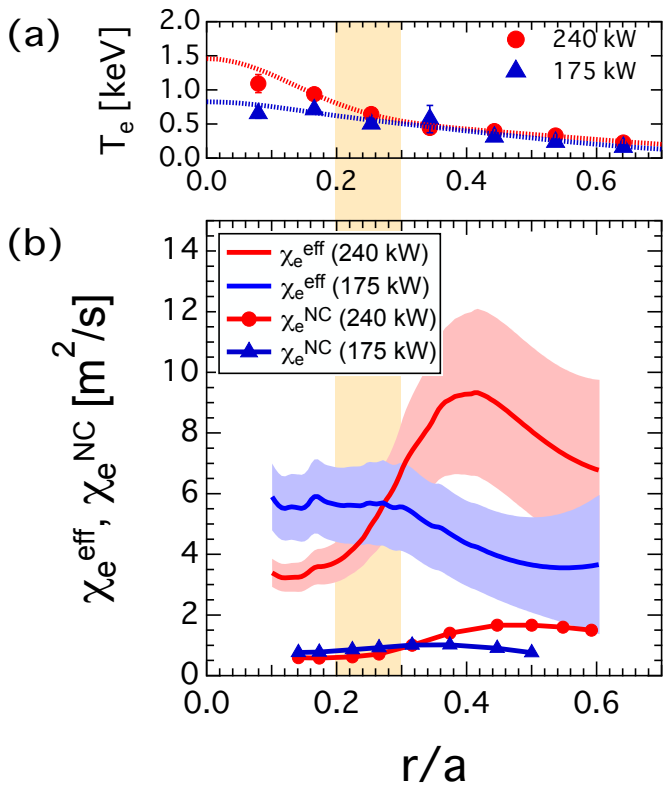

Figure 7. Radial profiles of (a) T_e and ECH deposition and (b) electron thermal diffusivity (χ_e^{eff}) and NC thermal diffusivity (χ_e^{NC}) for the peaked and non-peaked plasmas, respectively.

$\chi_e^{eff} \propto T_e^{-1.7}$. χ_e^{eff} outside the foot point scales roughly as $T_e^{3/2}$ (gyro-Bohm factor). Figure 8(b) shows the effective thermal diffusivity normalized by $T_e^{3/2}$ as a function of R/L_{T_e}. Here, R is the major radius of Heliotron J and L_{T_e} is the scale length of the radial T_e profile ($L_{T_e} = T_e/\nabla T_e$). Note that the thermal diffusivity in gyro-Bohm scaling is expressed as $\chi_{\mathrm{gyro-Bohm}} \propto T^{3/2}/B^2$[32]. The decrease in $\chi_e^{eff}/T_e^{3/2}$ suggests that inside the foot point, the heat transport does not depend on gyro-Bohm scaling. Outside the foot point, $\chi_e^{eff}/T_e^{3/2}$ values are constant regardless of the change in R/L_{T_e}. The $\chi_e^{eff}/T_e^{2/3}$ values inside the foot point are lower than those outside the foot point. $\chi_e^{eff}/T_e^{2/3}$ decreases as the T_e gradient increases, suggesting that the heat transport inside the foot point is smaller than that predicted by the T_e dependence of gyro-Bohm scaling.

In the previous section, we discussed the following topics that are recognized as the typical features of a helical eITB: (1) the reduction of thermal diffusivity, (2) the formation of a large positive E_r, (3) the transient formation with a threshold value, and (4) the reduction of turbulence. In Heliotron J, the reduction of the thermal diffusivity is predicted by the NC calculation. Experimental analysis in this section shows the reduction of the anomalous transport. Beam emission spectroscopy measurements[33]

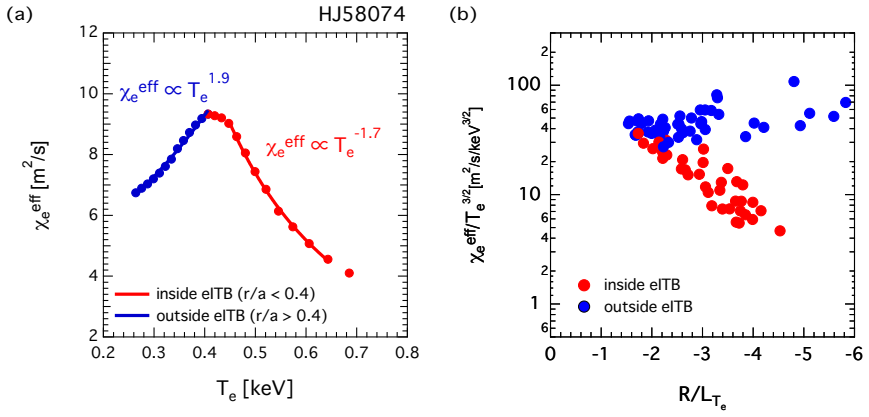

Figure 8. (a) Effective electron thermal diffusivity as a function of T_e inside and outside the foot point. (b) Normalized effective electron thermal diffusivity as a function of R/L_{T_e} inside and outside the foot point.

will be used in future studies to confirm the reduction of the turbulence. These characteristics are similar to those obtained from the NC theory and experimental observation in LHD, CHS, and W7-AS[19]. According to the discussions of (1)-(4), the peaked profile in Heliotron J is confirmed to be the eITB.

6. Hysteresis Feature of T_e between Back and Forth Transition

The temporal dynamics during the eITB formation are investigated. Figure 9(a) shows the time evolution of $\bar{n_e}$, W_p^{dia}, and $P_{\rm ECH}$. In this experiment, n_e is controlled to decrease until 210 ms and increase after that. The time evolution of T_e is obtained from the ECE diagnostic using a multichannel radiometer in the experiment. In the ECE measurement, the optical depth of the emission is greater than 2 within 30% of the plasma minor radius so that the radiation temperature corresponds to T_e near the core of Heliotron J. The time evolutions of T_e of $r/a \sim 0.1, 0.5$, and 0.95 are also shown in Fig. 9(b). The eITB was observed at 210 ms [Fig. 9(c)] in low n_e while it disappears at 260 ms [Fig. 9(d)] due to the increase in n_e. The time evolution of the ECE signal in the core region ($r/a \sim 0.1$) has the same tendency as the change in the T_e profile measured using YAG-TS. When n_e decreases, the ECE signal in the core region transiently increases at around 195 ms. When n_e increases, the ECE signal transiently decreases at around 235 ms. The eITB formed transiently and disappears at 195 and 235 ms. Figure 10 shows the trace of T_e at $r/a \sim 0.1$ as a function of $\bar{n_e}$. In this figure, we control n_e from the red arrow to the blue arrow. When T_e increase, $\bar{n_e} \sim 0.9 \times 10^{19}$ m^{-3}; however, when T_e decrease, $\bar{n_e} \sim 1.0 \times 10^{19}$ m^{-3}. Therefore, a hysteresis loop of the ECE signal for the n_e change is formed during the eITB formation. Due to hysteresis, the core T_e shows different values for the n_e decrease and n_e increase phases even at same n_e. This hysteresis indicates that after its formation, the eITB remains in the higher n_e plasma. In CHS, a bifurcation

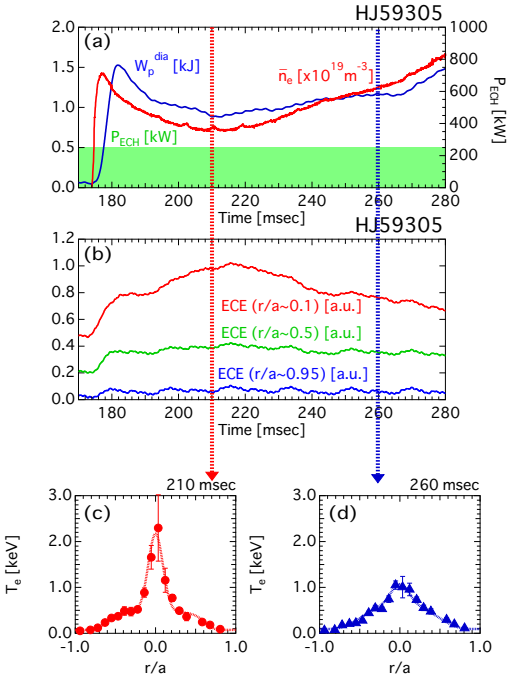

Figure 9. (a) Time evolution of the plasma stored energy and line-averaged electron density. (b)Time evolution of the electron cyclotron emission (ECE) signal (at $r/a \sim$ 0.1, 0.5, and 0.95). (c and d) T_e profiles at 210 ms and 260 ms.

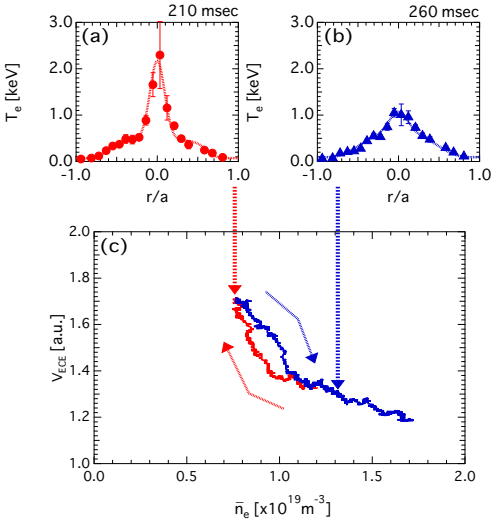

Figure 10. (a and b) T_e profiles at 210 and 260 ms. (c) Hysteresis of ECE signal on line-averaged electron density.

behavior is observed in the plasma potential measurement[34]. The hysteresis loop is ascribed to the local bifurcation nature predicted in the NC theory. It is suggested that the behavior of the ECE signal in Heliotron J is caused by the bifurcated E_r and that the thermal transport has the hysteresis feature.

7. Summary

The peaked T_e profile of Heliotron J has the following four features: (1) heat transport analysis shows the significant improvement of χ_e^{eff} in the plasma, with the eITB relative to that without the eITB. (2) Numerical calculations using the moment method predicts that a large positive E_r is formed in the core region. (3) When the value of $P_{\mathrm{ECH}}/\bar{n_e}$ exceeds the threshold of 250×10^{-19}kW m^3, both central T_e and the core T_e gradient increase transiently. (4) The large gap between χ_e^{eff} and χ_e^{NC} suggests that the suppression of anomalous thermal transport contributes to the core improved confinement of the eITB plasma. These features provide the evidence for the formation of an eITB in Heliotron J. Furthermore, the time evolution of the core T_e obtained by the ECE measurement shows the transient increase and hysteresis phenomena during the formation of the eITB.

Heliotron J is a suitable device for studying eITB physics with both various diagnostics and plasma control systems. We plan to measure E_r and a plasma flow via the CXRS. The ECH system of Heliotron J shows several advantages for the study of dynamics such as the hysteresis phenomena obtained by utilizing the continuous control of P_{ECH} during a single shot. The heat pulse thermal diffusivity will be evaluated by measuring the propagation of the heat pulses for eITB plasmas using a modulation ECH technique. In addition, we also plan to investigate the effect of the magnetic field configurations, such as a helical ripple and a magnetic island, on the mechanism of the eITB formation. This research is the first report of the eITB formation in the helical-axis heliotron configuration. The research of eITB physics in Heliotron J contributes to expand the variety of configuration research in stellarator/heliotron devices.

Acknowledgments

The authors acknowledge the Heliotron J technical staff for their great support. This research was partially supported by the NIFS Collaborative Research Program (NIFS10KUHK030, NIFS09KUHL, and NIFS10KUHL033) and JSPS KAKENHI Grant Number 15J09177.

References

[1] H. Maaβberg *et al.*, Physics of Plasmas **7** (2000) 295.
[2] A. Fujisawa *et al.*, Plasma Physics and Controlled Fusion **42** (2000) A103.
[3] Y. Takeiri *et al.*, Physics of Plasmas **10** (2003) 1788.
[4] F. Castejon *et al.*, Nuclear Fusion **42** (2002) 271.
[5] M. Yokoyama *et al.*, Fusion Science and Technology **50** (2006) 327-42.
[6] T. Shimozuma *et al.*, Fusion Science and Technology **58** (2010) 38.
[7] T. Minami *et al.*, Nuclear Fusion **44** (2004) 342-349.
[8] Y. Takeiri *et al.*, Fusion Science and Technology **50** (2004) 106.
[9] F. Castejon *et al.*, Nuclear Fusion **44** (2004) 593.
[10] T. Estrada *et al.*, Fusion Science and Technology **50** (2006) 127.

[11] F. Sano *et al.*, Plasma and Fusion Research **41** (2000) 26.
[12] T. Obiki *et al.*, Nuclear Fusion **41** (2001) 833.
[13] S.P. Hirshman *et al.*, Physics of Fluids **29** (1986) 2951-9.
[14] Van Rij *et al.*, Physics of Fluids **B 1** (1989) 563.
[15] A. Fujisawa *et al.*, Nuclear Fusion **41** (2001) 575.
[16] U. Stroth *et al.*, Physical Review Letters **86** (2001) 5910.
[17] N. Kenmochi *et al.*, Plasma and Fusion Research **8** (2013) 2402117.
[18] N. Kenmochi *et al.*, Review of Scientific Instrument **85** (2014) 11D819.
[19] M. Yokoyama *et al.*, Nuclear Fusion **47** (2007) 1213.
[20] T. Shimozuma *et al.*, Plasma Physics and Controlled Fusion **45** (2003) 1183.
[21] M. Yokoyama *et al.*, Fusion Science and Technology **50** (2006) 327.
[22] T. Minami *et al.*, Nuclear Fusion **44** (2004) 342.
[23] K. Ida *et al.*, Nuclear Fusion **56** (2016) 092001.
[24] T. Estrada *et al.*, Nuclear Fusion **56** (2016) 026011.
[25] C.D. Beidler *et al.*, Nuclear Fusion **51** (2011) 076001.
[26] K. Ida *et al.*, Physics of Plasmas **11** (2004) 2551.
[27] H.Y. Lee *et al.*, Plasma and Fusion Research **7** (2012) 1402019.
[28] J. Garcia *et al.*, Physical Review Letters **96** (2006) 105007.
[29] T. Tala *et al.*, Plasma Physics and Controlled Fusion **43** (2001) 507.
[30] N.B. Marushchenko *et al.*, Plasma and Fusion Research **2** (2007) S1129.
[31] K. Nagasaki *et al.*, Nuclear Fusion **51** (2011) 103035.
[32] J.W. Connor *et al.*, Plasma Physics and Controlled Fusion **30** (1988) 619.
[33] S. Kobayashi *et al.*, Review of Scientific Instrument **87** (2016) 11E519.
[34] A. Fujisawa *et al.*, Plasma Physics and Controlled Fusion **44** (2002) A1-A18.